Article ID: 1000-324X(2016)08-0881-09 **DOI:** 10.15541/jim20160015

Synthesis of Diatomite/g-C_3N_4 Composite with Enhanced Visible-light-responsive Photocatalytic Activity

WANG Dan-Jun[1], SHEN Hui-Dong[1], GUO Li[1, 2], HE Xiao-Mei[1], ZHANG Jie[1], FU Feng[1]

(1. School of Chemistry & Chemical Engineering, Shaanxi Key Laboratory of Chemical Reaction Engineering, Yan'an University, Yan'an 716000, China; 2. School of Materials Science & Engineering, Shaanxi Normal University, Xi'an 710119, China)

Abstract: Novel visible-light-responsive diatomite/g-C_3N_4 composite was successfully synthesized *via* a facile impregnation-calcination method. The sample was characterized by TG, XRD, FE-SEM, HR-TEM, FT-IR, XPS, UV-Vis-DRS, and PL spectra. The photocatalytic activities of samples were evaluated by degradation of RhB under visible light irradiation. Experimental results indicated that 2.32wt% diatomite/g-C_3N_4 composite exhibits high efficiency for the degradation of RhB. The photoreaction kinetics constant value is about 1.9 times as high as that of g-C_3N_4 under visible light irradiation. The radical trap experiments indicate that $\cdot O_2^-$ serves as the main active species for the photodegradation of RhB over 2.32wt% diatomite/g-C_3N_4 under visible light irradiation. The enhanced photoactivity is mainly attributed to the electrostatic interaction between g-C_3N_4 and negatively charged diatomite, synergistic effect lead to the efficient migration of the photogenerated electrons and holes of g-C_3N_4.

Key words: diatomite/g-C_3N_4 composite; impregnation-calcination method; visible-light-irradiation; electrostatic interaction

Up to now, it is still a difficult problem to treat dyes wastewater due to its high stability and complicated compositions. The conventional treatment methods, such as absorption, ultrafiltration, reverse osmosis, coagulation, *etc*. are ineffective for its decolorization and mineralization[1]. In order to cope with the growing environmental problems, new efficient environment purification technologies have been developed, such as advanced oxidation processes[2]. Photocatalytic technology is an efficient means which is applicable on completely degrading organic pollutants in waste water but very challenging process to convert solar energy into chemical energy[3]. So, it is urgent and indispensable to utilize sunlight efficiently, development of more efficient, sustainable, visible-light-responsive photocatalytic materials.

Recently, graphitic carbon nitride (g-C_3N_4) which is a metal-free polymeric photocatalyst, have attracted extensive attention because of its good photocatalytic performance for hydrogen or oxygen production *via* water splitting under visible light irradiation[4]. In general, the preparation of g-C_3N_4 obtained by heating low-cost melamine was investigated by Zou's group[5]. The metal free g-C_3N_4 photocatalyst possesses very high thermal, optical, chemical stability and exceptional electronic as well as biocompatible properties[6], which make it valuable for photocatalytic applications. However, the photocatalytic performance of g-C_3N_4 has been restricted due to its optical moderate band gap (E_g=2.7 eV) and the high recombination rate of photogenerated electron hole pairs[7]. Therefore, scientists have made significant efforts to improve the photocatalytic activity of g-C_3N_4. To this end, various strategies have been developed, such as doping with metal/nonmetal elements[8-11], formation of heterosjunction (*e.g.* CdS/g-C_3N_4[12], $SmVO_4$/g-C_3N_4[13], N-TiO_2/g-C_3N_4[14], g-C_3N_4/Ag_3PO_4 [15], $DyVO_4$/g-C_3N_4[16], *etc.*), isotype heterostructure and noble metal modification[17-18]. Up to now, it is still a challenge to construct g-C_3N_4 based photocatalyst with efficient utilization of visible light, suitable band edges for targeted reactions, high stability, environmental friendliness, and low cost materials to modify g-C_3N_4.

Diatomite is a naturally formed non-metallic siliceous sedimentary material[19]. Due to its high porosity, specific surface area, high adsorption capability, cheap, abundant, non-toxic and environmental friendly, diatomite represents an attractive substrate for immobilization of variety of photocatalysts[20-22]. Compared with other clay, it has

Received date: 2016-01-06; **Modified date:** 2016-01-22
Foundation item: National Natural Science Foundation of China (21373159); Project of Science & Technology Office of Shananxi Province (2015SF291, 2013K11-08, 2013SZS20-P01); Shaanxi Provincial Education Department Found (15JS119)
Biography: WANG Dan-Jun(1976–), male, PhD, associate professor. E-mail: wangdj761118@163.com

natural ordered micro-/macroporous structures, high adsorption capacity and possesses abundant adsorption sites. These advantages make diatomites to be one of the most promising adsorption materials in processing wastewater[23-25]. Furthermore, studies have confirmed that diatomites is a good matrix for synthesizing composite photocatalysts with higher photocatalytic activity, such as TiO_2/diatomite[26-27], (PEG)/diatomite[28], Ce-TiO_2/diatomite[29], and PCM/diatomite[30].

Recently, Wang and co-worked reported that MoS_2 with layered structure can promote the photocatalytic activity of g-C_3N_4[31]. Very recently, Li *et al*[32] reported the bentonite/g-C_3N_4, which exhibited a significantly enhancement photocatalytic activity, Si–OH on the surface of layered bentonite can form strong forces with g-C_3N_4, which allow the prompt migration of light-induced charge. Herein, in view of the similar structure and composition of diatomite and bentonite, a impregnation-calcination route was employed to synthesize the novel visible-light-responsive diatomite/g-C_3N_4 composite. The photodegradation experiments were performed and the possible mechanisms of enhancement of diatomite/g-C_3N_4 composite were also investigated.

1 Materials and methods

1.1 Sample preparation

All reagents were of analytical purity and were used without further purification. In a typical procedure, 1.0 g of diatomite was placed in a plastic beaker and mixed with 20 mL of 2.0 mol/L NaOH solution under magnetic stirring. After reaction for 12 h at ambient temperature, the sample was collected and washed until achieving pH of the solution was 7.0, then dried at 80℃ overnight, and ground into a powder in a mortar. The obtained product was denoted treated diatomite.

Synthesis of diatomite/g-C_3N_4. Firstly, in order to obtain well dispersed diatomite sheets, a certain amount of diatomite (0.01 g, 0.02 g, 0.04 g, 0.10 g, 0.20 g) was dispersed in 30 mL methyl alcohol with 30 min continuous ultrasonic at room temperature. Subsequently, 4.0 g melamine was added to the diatomite suspension with stirring at 25℃ for 4 h. Then, the mixture was dried at 70℃ for 6 h and the resulting dried mixtures were calcinated at 550℃ for 4 h in a muffle furnace. The obtained products are grayish yellow, which were obtained from six reactant systems. According to thermogravimetric analysis (TG) results, the weight contents of diatomite in diatomite/g-C_3N_4 composites were estimated to be 1.22wt%, 2.32wt%, 5.46wt%, 13.88wt% and 25.21wt%, respectively. Bulk g-C_3N_4 was also prepared according to the similar above process. Based on the TG result of 2.32wt%diatomite/g-C_3N_4 composite, diatomite and g-C_3N_4 mechanical mixture were prepared by mixing diatomite (0.01 g) with g-C_3N_4 (0.55 g), which was denoted as diatomite/g-C_3N_4 mixture. In addition, diatomite/g-C_3N_4 (2.32wt%) sample was also prepared by using diatomite without alkali treated as material, and the resulted sample was denoted as untreateddiatomite/g-C_3N_4 (2.32wt%).

1.2 Characteration

The crystalline phases of diatomite/g-C_3N_4 composites were analyzed by XRD using a Shimadzu XRD-7000 X-ray diffractometer (CuKα, 0.15418 nm). The morphologies and structure of the obtained samples were examined by FE-SEM (JSM-6700F) and HR-TEM (JEM-2100). FT-IR spectra of samples were recorded on a Nicolet Avatar-370 spectrometer at room temperature. The UV-Vis diffuse reflection spectra (UV-Vis-DRS) of the samples were measured using a Shimadzu UV-2550 UV-Vis spectrophotometer. $BaSO_4$ was used as the reflectance standard. X-ray photoelectron spectroscopy (XPS) analysis was performed on an ESCA Lab MKII X-ray photoelectron spectrometer. TG analysis was done on STA-449C Jupiter (NETZSCH Corporation, Germany).

1.3 Photocatalytic experiment

The photocatalytic activities of diatomite/g-C_3N_4 were evaluated by using RhB as a model pollutant under irradiation of a 400 W metal halide lamp with an optical filter to cut off the light below 420 nm. In a typical process, 200 mg of photocatalyst and 200 mL RhB solution was stirred in dark for 1.0 h to establish an adsorption/desorption equilibrium. At interval of 10 min, 10 mL solution was sampled and centrifuged to remove the catalyst particles. The concentration was analyzed by measuring the maximum absorbance at 554 nm for RhB using a Shimadzu UV-2550 spectrophotometer. In order to further investigate the active species involved in the photocatalytic process, a series of quenching tests have been performed. EDTA-2Na (ethylenediamine tetraacetic acid disodium salt), IPA (isopropanol), BQ (p-benzoquinone) was used as a quencher for holes (h^+), hydroxyl radicals (·OH) and superoxide radical ($\cdot O^{2-}$), respectively[33]. The concentration of quencher is 1 mmol/L in the solution.

2 Results and discussion

2.1 XRD, XPS and TG analysis

Fig. 1 shows the powder XRD patterns of raw diatomite, alkali treatment diatomite, g-C_3N_4 and various diatomite/g-C_3N_4 composites. As can be seen from Fig. 1(a), two marked peaks can be ascribed to (100) and (002)

characteristic diffraction planes of the g-C_3N_4[5-6]. For the diatomite clay, the XRD pattern of raw diatomite revealed that the main phase of non-crystalline opal-A with the characteristic broad peak centered at the peak of 21.8°[24]. The XRD pattern of alkali treatment diatomite was similar to that of raw diatomite, indicating that the NaOH etching did not alter the diatomite mineral structure. In the case of diatomite/g-C_3N_4 composites, crystalline diatomite is not obviously observed with low diatomite loadings. However, in the enlarged Fig. 1(b) from 25°to 30°, the as-prepared diatomite/g-C_3N_4 composites with higher diatomite loadings (>2.32%), the peak intensity corresponding to (002) lattice plane decreased. This result suggested that the diatomite/g-C_3N_4 composites are constituted by *g*-C_3N_4 and diatomite.

To investigate the valence states of various species, the diatomite/g-C_3N_4 (2.32wt%) was studied by X-ray photoelectron spectroscopy (XPS). XPS results indicate the presence elements of Si, C, N and O in the diatomite/g-C_3N_4 (2.32wt%) composite (Fig. 2(a)). The C1s characteristic peaks at 288.08 eV and 284.58 eV, as shown in Fig. 2(b), are assigned to C–N–C coordination and the adventitious carbon, respectively[9]. Fig. 2(c) shows the N1s binding energy of g-C_3N_4 at 398.78 eV, which is assigned to nitrogen element of sample[9]. Both C1s and N1s binding energies of 2.32wt% diatomite/g-C_3N_4 show minor negative shifts compared to pure g-C_3N_4, indicating there exist the interaction force between diatomite and g-C_3N_4.

Fig. 3 shows the weight loss of diatomite is negligible, which indicating very few residual water and organic impurities exist in diatomite, and the dehydroxylation of aluminosilicate is slightly. As for diatomite/g-C_3N_4 composites, they have no obvious difference in the thermal stability. The initial decomposition temperature of diatomite/g-C_3N_4 composites is at about 545℃, which is lower than that of g-C_3N_4 at 550℃. The reason may be attributed to the existence of fluffy sheets of g-C_3N_4 in the composites. However, the complete decomposition temperature of diatomite/g-C_3N_4 composites is at about 710℃, which is almost equal to that of g-C_3N_4. The quality score of diatomite was almost close to the theoretical calculated value of diatomite/g-C_3N_4, for example (Table 1).

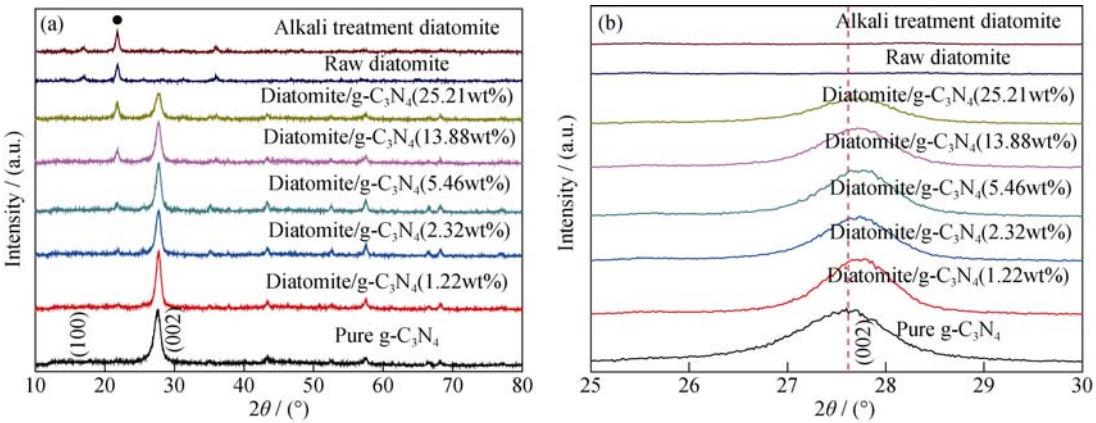

Fig. 1　XRD patterns of samples

(a) XRD patterns of diatomite, *g*-C_3N_4 and diatomite/g-C_3N_4 composite; (b) Enlarged XRD pattern of diatomite g-C_3N_4 and diatomite/g-C_3N_4 composites from 25° to 30°

The peaks marked by (●) in (a) are the characteristic of the Quartz impurity in the diatomite sample

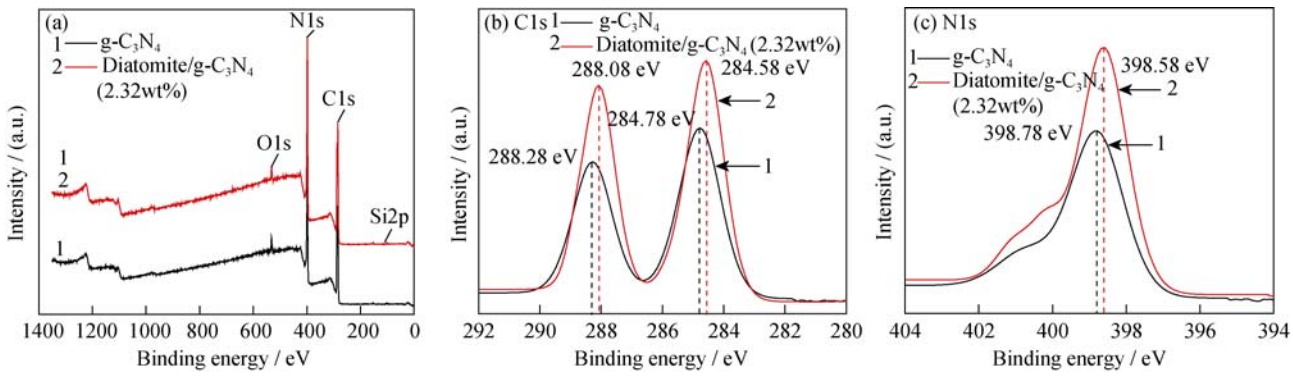

Fig. 2　XPS spectra of g-C_3N_4 and diatomite/g-C_3N_4(2.32wt%)

(a) Survey spectra; (b) C1s; (c) N1s

Table 1 Content in diatomite/g-C_3N_4 by TG curves analysis

Samples	Diatomite theoretical content /wt%	Diatomite experimental/wt%
Diatomite/g-C_3N_4 (1.22wt%)	1.79	1.22
Diatomite/g-C_3N_4 (2.32wt%)	3.56	2.32
Diatomite/g-C_3N_4 (5.46wt%)	6.78	5.46
Diatomite/g-C_3N_4 (13.88wt%)	15.38	13.88
Diatomite/g-C_3N_4 (25.21wt%)	26.67	25.21

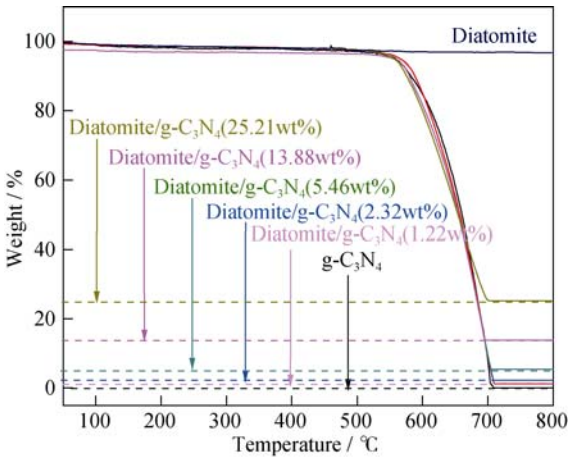

Fig. 3 TG curves for heating diatomite, g-C_3N_4 and diatomite/g-C_3N_4 composites

2.2 Morphology and structure analysis

Fig. 4 shows the size and morphology of g-C_3N_4, raw diatomite, alkali treatment diatomite and diatomite/g-C_3N_4 composites. It can be seen that diatomite sample has disk-like and highly developed macroporous structure. After NaOH washing, the morphology of raw diatomite was preserved, while the size of the central macropores increased (Fig. 4(a)-(b)). After diatomite loading onto the surface of layered g-C_3N_4, the diatomite/g-C_3N_4 composite can be observed with abundant fluffy sheets (Fig. 4(c)). Fig. 4(d) is the TEM image of 2.32wt%diatomite/g-C_3N_4. It can be clearly observed that some diatomite particles was loaded on the surface of layered structure g-C_3N_4. In HR-TEM image(Fig. 4(f)), the border of diatomite and g-C_3N_4 can be observed clearly, suggesting diatomite layers combining well with g-C_3N_4.

Fig. 5 shows the FT-IR spectra of diatomite, g-C_3N_4, and diatomite/g-C_3N_4 composites. As can be seen from Fig. 5, the intense peaks in the FTIR spectrum at 1629 cm^{-1}, 1105 cm^{-1}, 796 cm^{-1} and 467 cm^{-1} are observed for the raw diatomite, which are related to the structure of diatomite, the peak at 1105 cm^{-1} is due to vibration siloxane linkages Si–O–Si[34]. The band at 1629 cm^{-1} reflects H–O–H bonding vibration of structured water molecules of silica. The peaks observed at 796 cm^{-1} is assigned to vibration in the silica structure of the symmetric external Si–O bond[35]. According to Elze and Rice's report[36], occurrence of the band with a maximum at 467 cm^{-1} is characteristic of the

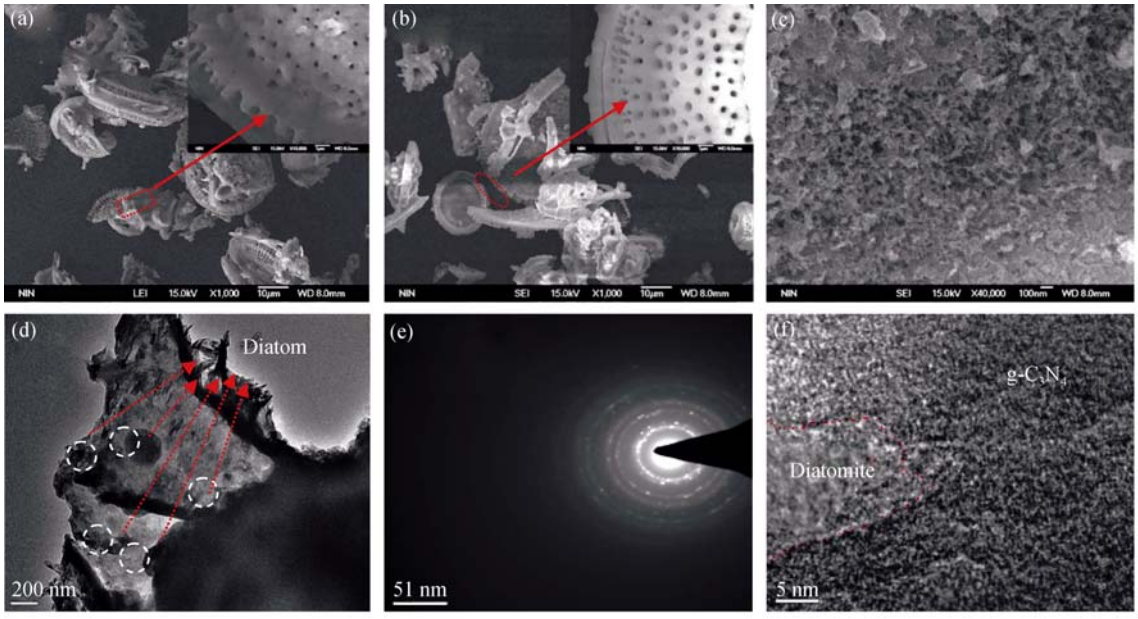

Fig. 4 FE-SEM and TEM images of samples

(a) FE-SEM image of diatomite; (b) FE-SEM image of alkali washed diatomite; (c) FE-SEM image of diatomite/g-C_3N_4 composite; (d) TEM of diatomite/g-C_3N_4 composite; (e) SEAD pattern of g-C_3N_4; (f) Conjunction edge between flake-like g-C_3N_4 and diatomite particles

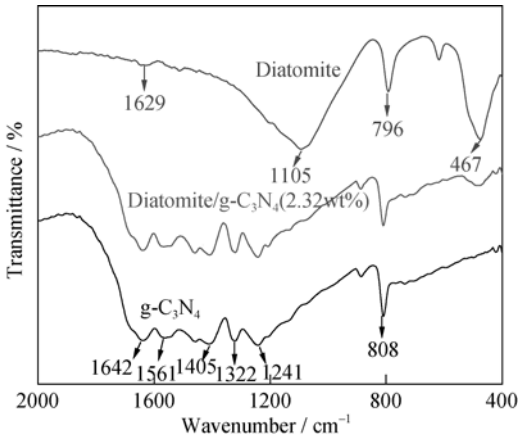

Fig. 5 FT-IR spectra of diatomite, g-C_3N_4 and diatomite/g-C_3N_4 composites

Si–O bonds in silica minerals such as tridymite and cristobalite. All these characteristic peaks suggest that diatomite is mainly composed of SiO_2. For the g-C_3N_4 sample, peaks positions between 1200 and 1650 cm^{-1} regions are related to the stretching modes of CN heterocycles[37]. The peaks at 1642 cm^{-1} and 1561 cm^{-1} ascribed to the C≡N stretching vibrations modes[38], while the peaks at 1241 cm^{-1}, 1322 cm^{-1} and 1405 cm^{-1} to the aromatic C–N strechings[39]. The peak located at 808 cm^{-1} was related to the characteristic breathing mode of triazine units[40]. In the case of diatomite/g-C_3N_4 composites, the wide band with intense absorption observed at 467 cm^{-1} is characteristic of the Si–O bonds in silica minerals. The FT-IR results indicate that this diatomite/g-C_3N_4 composites contains two fundamental components of diatomite and g-C_3N_4 and that no appreciable chemical reaction occurred between diatomite and g-C_3N_4.

2.3 UV-Vis-DRS analysis

Fig. 6 shows the UV-Vis-DRS spectra of pure g-C_3N_4 and diatomite/g-C_3N_4 composites. In Fig. 6(a), the absorption edge of pure g-C_3N_4 was estimated to be 470 nm and exhibited a strong absorption ability in the visible-light region. It can also be clearly seen that diatomite/g-C_3N_4 composites with different diatomite contents show different absorption abilities as compared with pure g-C_3N_4, indicating that there may be some interaction between diatomite and g-C_3N_4. In previous TEM analysis, the diatomite/g-C_3N_4 composites show enlarged much fluffy layer structure. In view of the partly imperfect polymer-like structure of g-C_3N_4[41], the g-C_3N_4 in diatomite/g-C_3N_4 might have more defects compared with the pure g-C_3N_4, which improves the utilization of light energy. The band gap energy (E_g) of samples can be estimated from the plots of $(\alpha h\nu)^{1/2}$ *vs* photon energy (Fig. 6(b)). Therefore, the visible light responses of diatomite/g-C_3N_4 composites are significant improved.

2.4 Photocatalytic activity

Fig. 7(A) shows the photocatalytic activity of samples for the degradation of RhB under visible light irradiation. It was found that RhB self-degradation was negligible, diatomite/g-C_3N_4 (2.32wt%) and diatomite/g-C_3N_4 (5.46wt%) exhibited higher photocatalytic activity than that of g-C_3N_4. After irradiation for 30 min, the photocatalytic degradation rate of RhB was 98.94% and 91.00% for for diatomite/g-C_3N_4 (2.32wt%) and pure g-C_3N_4, respectively. The photocatalytic activity of diatomite/g-C_3N_4 improved with increasing diatomite content, and the optimal diatomite content was 2.32wt%. The photocatalytic activity of diatomite/g-C_3N_4 mixture, untreated and treated diatomite/g-C_3N_4 (2.32wt%) was compared and listed in Fig. 7(B). It was clearly observed that diatomite/g-C_3N_4 (2.32wt%) sample exhibited the highest degradation. It may be ascribed to two reasons: firstly, alkali treatment can improve the specific surface area of diatomite, which is beneficial to absorb the RhB; secondly, alkali treatment can enhance the electrostatic interaction of g-C_3N_4 and diatomite. When g-C_3N_4/diatomite is dispersed in water, Na^+ diffused away from the solid surface and left the negative charges on the diatomite surface. The negatively charged of diatomite can promote the immigration of electrons and holes, thus suppress the charge recombination. The alkali treated diatomite possesses more Na^+ than that of untreated diatomite, which results in the treated diatomite/g-C_3N_4 showing higher degradation than that of untreated one.

Fig. 7(C) showed that the pseudo first order rate constant (k) for RhB degradation with g-C_3N_4 was 0.07618 min^{-1}. For diatomite/g-C_3N_4 composites with diatomite contents of 1.22wt%, 2.32wt%, 5.46wt%, 13.88wt%, 25.21wt% and diatomite/g-C_3N_4 mixture, the corresponding k value were calculated to be 0.07758, 0.14239, 0.10701, 0.03183, 0.02353, and 0.06089 min^{-1}, respectively. In the diatomite/g-C_3N_4 composites, the k value of diatomite/g-C_3N_4 (2.32wt%) is 1.9 times as high as that of the pure g-C_3N_4. However, further increasing the proportion of diatomite, the k value shows a slight decrease due to the shading effect. Therefore, excess loading of diatomite could prevent g-C_3N_4 from absorbing the light and result in a deceasing of catalytic activity. It can be seen from Fig. 7(D) that the absorptive property of diatomite/g-C_3N_4 increase remarkably with increasing diatomite content. However, the adsorption capacity of diatomite/g-C_3N_4 composites is not superior to that of diatomite and g-C_3N_4 mixture. It is obvious that the enhanced photocatalytic activity of diatomite/g-C_3N_4 composites is not ascribed to the adsorption capability. The significant differences in the interface of the composite is responsible for the enhanced photocata-

lytic activity of diatomite/g-C_3N_4 composite[32].

Fig. 7(E) shows temporal evolution of the spectral changes during photocatalytic degradation of RhB over diatomite/g-C_3N_4 (2.32wt%) composite. It can be seen that the intensity of the absorption peak decrease drastically within 30 min. On the other hand, from the viewpoint of practical application, it is important to evaluate the stability of the diatomite/g-C_3N_4 catalyst. The repeated experiment results indicated that the photocatalytic activity of 2.32wt%diatomite/g-C_3N_4 composite showed negligible decreasing after five cycles and the crystal structure didn't not change after the photocatalytic reaction(Fig. 7(F)).

2.5 Photocatalytic mechanism

Generally speaking, PL spectra analysis was a reliable method to investigate the fate of photogenerated electrons and holes[42]. Therefore, in present study, PL spectrum was

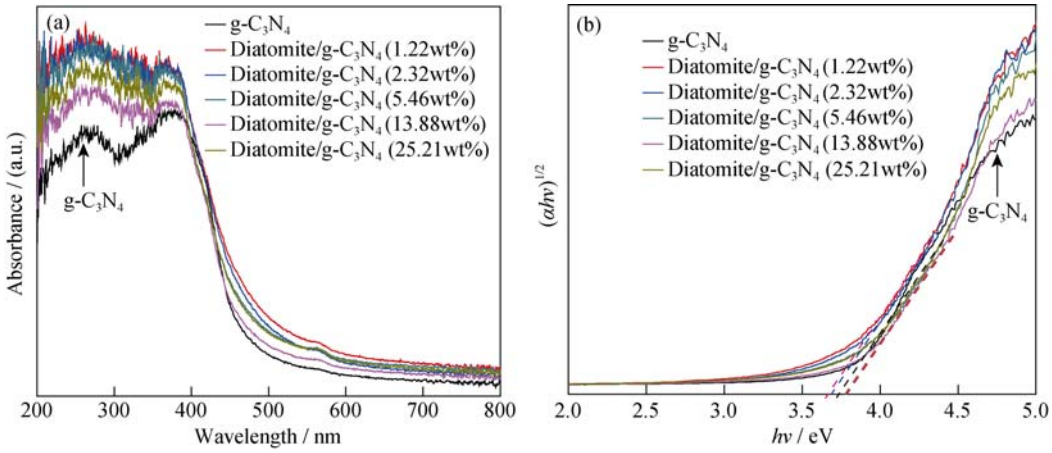

Fig. 6 (a) UV-Vis spectra and (b) plot of $(\alpha h\nu)^{1/2}$ *vs* energy (hν) for the band gap energy of g-C_3N_4 and diatomite/g-C_3N_4 composites

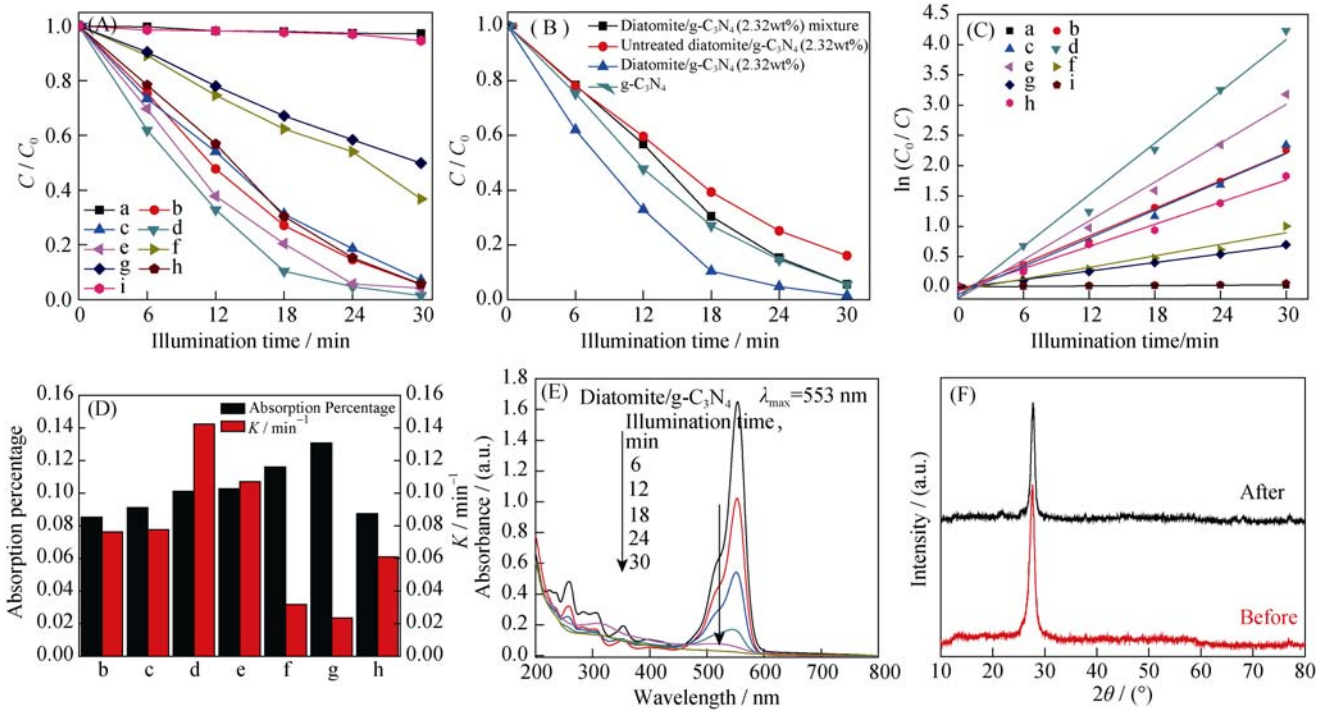

Fig. 7 Photocatalytic activity of the samples

(A) Photocatalytic degradation efficiency of RhB by g-C_3N_4 and diatomite/g-C_3N_4 composites; (B) Comparison of mixted, treated and untreated diatomite/g-C_3N_4(2.32wt%); (C) Kinetic fit for the degradation of RhB with g-C_3N_4 and diatomite/g-C_3N_4 composites (a, blank; b, g-C_3N_4; c, diatomite/g-C_3N_4 (1.22wt%); d, diatomite/g-C_3N_4 (2.32wt%); e, diatomite/g-C_3N_4 (5.46wt%); f, diatomite/g-C_3N_4 (13.88wt%); g, diatomite/g-C_3N_4 (25.21wt%); h, diatomite/g- C_3N_4 mixture (2.32wt%); i, diatomite); (D) Adsorption percentage and rate constants; (E) Absorption spectral changes of RhB under visible light irradiation using diatomite/g-C_3N_4 (2.32wt%) as photocatalyst; (F) XRD patterns of diatomite/g-C_3N_4 before and after being used

employed to further verify the interfacial charge transfer dynamics between the hetero-geneous interface of pure g-C_3N_4 and the diatomite/g-C_3N_4 composites. As can be seen in Fig. 8, for the pure g-C_3N_4, one main emission peak appears at about 470 nm, which is attributed to the inner band gap of g-C_3N_4[4]. After introducing diatomite onto g-C_3N_4, the intensities of the PL signal for the diatomite/g-C_3N_4 composites are lower than that of g-C_3N_4, indicating that the composites have a lower recombination rate of electrons and holes under visible-light irradiation. As a consequence, it is reasonable to conclude that diatomite loading can enhance photocatalytic activity of g-C_3N_4.

In addition, BQ, EDTA-2Na, and IPA were used as quenchers for $\cdot O_2^-$, holes (h^+), and ·OH scavengers, respectively[43-44]. Fig. 9 shows the active species trapping experiment in photocatalytic process of diatomite/g-C_3N_4 (2.32wt%) composite. The experimental results indicated that the photodegradation of RhB was almost not affected by adding EDTA-2Na as quencher of h^+, respectively. While IPA slightly suppressed the photocatalytic degradation of RhB. Nevertheless, the activity of the diatomite/g-C_3N_4 (2.32wt%) composite was largely suppressed by the addition of BQ. Thus, it could be inferred that $\cdot O_2^-$ serve as the main active species for the photodegradation of RhB over diatomite/g-C_3N_4 (2.32wt%) under visible light irradiations, and the reaction was partly driven by the action of ·OH radicals. Considering the above results, ·OH, $\cdot O_2^-$were established as the main reactive species for RhB degradation, as depicted in the following formule:

$$\text{diatomite/g-}C_3N_4 + h\gamma \rightarrow \text{diatomite/g-}C_3N_4(e^- + h^+) \quad (1)$$

$$e^- + O_2 \rightarrow \cdot O_2^- \quad (2)$$

$$2e^- + O_2^- + 2H^+ \rightarrow \cdot OH + OH^- \quad (3)$$

$$RhB + \cdot O_2^- / \cdot OH / \rightarrow CO_2 + H_2O + ... \quad (4)$$

As discussed above, three main reasons for the increase in the photocatalytic efficiency of coupled g-C_3N_4/diatomite composites are: (i) the absorption edges of diatomite/g-C_3N_4 composites shift significantly to longer wavelengths compared with the pure g-C_3N_4, which indicates the composites can be excited by more visible light photons; (ii) the improved adsorptive activity of diatomite/g-C_3N_4 composites compared with that of g-C_3N_4; (iii) the electrostatic interaction, the negatively charged of diatomite can promote the immigration of electrons and holes, thus suppresses the charge recombination.

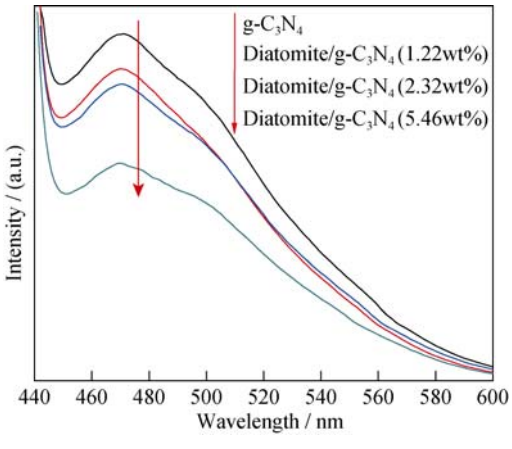

Fig. 8　PL spectra of g-C_3N_4 and diatomite/ g-C_3N_4 composites

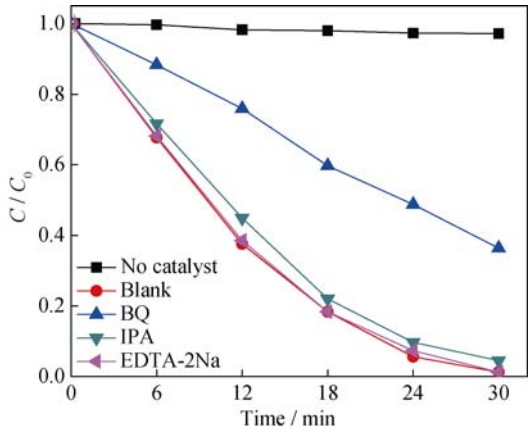

Fig. 9 Trapping experiment of active species during photocatalytic degradation of RhB over diatomite/g-C_3N_4 (2.32wt%) under visible light irradiation

When g-C_3N_4/diatomite is dispersed in water, Na^+ diffused away from the solid surface the exchangeable cations and left the negative charges on the diatomite surface. Under visible light irradiation, only g-C_3N_4 can be activated, the e^-/h^+ pairs of g-C_3N_4 should present on the g-C_3N_4 surface. The excited electrons and holes of g-C_3N_4 should be driven to migrate efficiently due to electrostatic interaction between g-C_3N_4 and the negatively charged diatomite. Thus, the charge recombination could be easily suppressed, leaving more charge carriers and enhancing the photocatalytic activity. Driven by the calcinations process, the layers of diatomite and g-C_3N_4 are splitted into many fluffy and thin sheets and a tight contact of diatomite with g-C_3N_4 can be achieved[45-46]. Therefore, the high photoactivity of diatomite/g-C_3N_4 composite arises from the synergistic effects between diatomite and g-C_3N_4 interfaces.

3　Conclusions

A novel visible-light-responsive diatomite/g-C_3N_4 composite was successfully synthesized *via* a facile impregnation-calcination method. Photocatalytic experimental result indicated that diatomite/g-C_3N_4 composites exhibited higher photocatalytic activity than pure g-C_3N_4 in the degradation of RhB. The radical trap experiments showed that the degradation of RhB was driven mainly by

the $\cdot O_2^-$, and partly by the action of ·OH radicals. The significant enhancement in the photocatalytic performance of diatomite/g-C_3N_4 composites is ascribed not only to its adsorptivity but also to the interaction between g-C_3N_4 and diatomite, this can promote the efficient migration of the photogenerated electrons and holes of g-C_3N_4 and consequently improves the photocatalytic activity. This strategy is expected to be extended to other g-C_3N_4 loaded materials, which might have potential applications in removing pollutant.

References:

[1] KONSTANINOU I K, ALBANIS T A. TiO_2-assistd photocatalytic degradation of azo dyes in aqueous solution: kinetic and mechanistic investigations. *Appl. Catal. B*, 2004, **49(1):** 1–14.

[2] ARSLAN A I, TURELII G, OLMEZ H T. Treatment of zao dye production wastewaters using Photo-fenton-like advanced oxidation process: optimization by response surface methodology. *J. Photochem. Photobiol. A*, 2009, **202(2/3):** 142–153.

[3] WALTER M G, WARREN E L, MCKONE J R, *et al*. Solar water splitting cells. *Chem. Rev*., 2010, **110(11):** 6446–6473.

[4] WANG X C, MAEDA K, THOMAS A, *et al*. A metal-free polymeric photocatalyst for hydrogen production from water under visible light. *Nat. Mater.,* 2009, **8(1):** 76–80.

[5] YAN S C, LI Z S, ZOU Z G. Photodegradation performance of g-C_3N_4 fabricated by directly heating melamine. *Langmuir*, 2009, **25(17):** 10397–10401.

[6] ZHANG X D, XIE X, WANG H, *et al*. Enhanced photoresponsive ultrathin graphitic-phase C_3N_4 nanosheets for bioimaging. *J. Am. Chem. Soc.,* 2013, **135(1):** 18–21.

[7] ZHANG Y, MORI T, YE J, *et al*. Phosphorus-doped carbon nitride solid: enhanced electrical conductivity and photocurrent generation. *J. Am. Chem. Soc.,* 2010, **132(18):** 6294–6295.

[8] MA X G, LV Y H, XU J, *et al*. A strategy of enhancing the photoactivity of g-C_3N_4 *via* doping of nonmetal elements: a first- principles study. *J. Phys. Chem. C*, 2012, **116(44):** 23485–23493.

[9] YAN S C , LI Z S, ZOU Z G. Photodegradation of rhodamine B and methyl orange over boron-doped *g*-C_3N_4 under visible light irradiation. *Langmuir,* 2010, **26(6):** 3894–3901.

[10] WANG Y, ZHANG J, WANG X, *et al*. Boron-and fluorine-containing mesoporous carbon nitride polymers: metal-free catalysts for cyclohexane oxidation. *Angew. Chem. Int. Ed.,* 2010, **49(19):** 3356–3359.

[11] CHEN X F, ZHANG J S, FU X Z, *et al*. Fe-g-C_3N_4-catalyzed oxidation of benzene to phenol using hydrogen peroxide and visible light. *J. Am. Chem. Soc.,* 2009, **131(33):** 11658–11659.

[12] GE L, ZUO F, LIU J K, *et al*. Synthesis and efficient visible light photocatalytic hydrogen rvolution of polymeric g-C_3N_4 coupled with CdS quantum dots. *J. Phys. Chem. C*, 2012, **116(25):** 13708–13714.

[13] LI T T, ZHAO L H, HE Y M, *et al*. Synthesis of g-C_3N_4/$SmVO_4$ composite photocatalyst with improved visible light photocatalytic activities in RhB degradation. *Appl. Catal. B*, 2013, **129:** 255–263.

[14] WANG X J, YANG W Y, LI F T, *et al*. *In situ* microwave-assisted synthesis of porous N-TiO_2/g-C_3N_4 heterojunctions with enhanced visible-light photocatalytic properties. *Ind. Eng. Chem. Res*., 2013, **52(48):** 17140–17150.

[15] KATSUMATA H, SAKAI T, SUZUKI T, *et al*. Highly efficient photocatalytic activity of g-C_3N_4/Ag_3PO_4 hybrid photocatalysts through Z-scheme photocatalytic mechanism under visible light. *Ind. Eng. Chem. Res.*, 2014, **53(19):** 8013–8025.

[16] HE Y M, CAI J, LI T T, *et al*. Synthesis, characterization, and activity evaluation of $DyVO_4$/g-C_3N_4 composites under visible-light irradiation. *Ind. Eng. Chem. Res*., 2012, **51(45):** 14729–14737.

[17] DONG F, NI Z L, LI P D, *et al*. A general method for type I and type II g-C_3N_4/g-C_3N_4 metal-free isotype heterostructures with enhanced visible light photocatalysis. *New J. Chem.*, 2015, **39(6):** 4737–4744.

[18] GE L, HAN C, LIU J, *et al*. Enhanced visible light photocatalytic activity of novel polymeric g-C_3N_4 loaded with Ag nanoparticles. *Appl. Catal. A*, 2011, **409–410:** 215–222.

[19] JUNG K W, JANG D, AHN K H. A novel approach for improvement of purity and porosity in diatomite (diatomaceous earth) by applying an electric field. *Int. J. Miner. Process*, 2014, **131:** 7–11.

[20] WANG B, ZHANG G X, LENG X. Characterization and improved solar light activity of vanadium doped TiO_2/diatomite hybrid catalysts. *J. Hazard. Mater*., 2015, **285:** 212–220.

[21] SUN Z M, YANG X P, ZHANG G X, *et al*. A novel method for purification of low grade diatomite powders in centrifugal fields. *Int. J. Miner. Process,* 2013, **125:** 18–26.

[22] LOSIC D, MITCHELL J G, VOELCKER N H. Diatomaceous lessons in nanotechnology and advanced materials. *Adv. Mater.,* 2009, **21(29):** 2947–2958.

[23] SPRYNSKYY M, KOVALCHUK I, BUSZEWSKI B. The separation of uranium ions by natural and modified diatomite from aqueous solution. *J. Hazard. Mater.,* 2010, **181(1/2/3):** 700–707.

[24] YU W B, YUAN P, LIU D, *et al*. Facile preparation of hierarchically porous diatomite/MFI-type zeolite composites and their performance of benzene adsorption: The effects of NaOH etching pretreatment. *J. Hazard. Mater.,* 2015, **285:** 173–181.

[25] DU Y C, FAN H G, WANG L P, *et al*. α-Fe_2O_3 nanowires deposited diatomite: highly efficient absorbents for the removal of arsenic. *J. Mater. Chem. A*, 2013, **1(26):** 7729–7737.

[26] PADMANABHAN S K, PAL S, HAQ E U, *et al*. Nanocrystalline TiO_2-diatomite composite catalysts: effect of crystallization on the photocatalytic degradation of rhodamine B. *Appl. Catal. A: Gen.,* 2014, **485:** 157–162.

[27] XIA Y, LI F F, JIANG Y S, *et al*. Interface actions between TiO_2 and porous diatomite on the structure and photocatalytic activity of TiO_2-diatomite. *Appl. Surf. Sci.,* 2014, **303:** 290–296.

[28] KARAMAN S, KARAIPEKLI A, ALPER B A. Polyethylene glycol (PEG)/diatomite composite as a novel form-stable phase change material for thermal energy storage. *Solar Energy Mater.*

Solar Cells, 2011, **95:** 1647–1653.

[29] LIANG X H, FU X Y. Effect of the Ce-TiO_2/diatomite on the photo-catalysis degradation of MB. *Mater. Sci. Forum.,* 2014, **789:** 44–47.

[30] JEONG S G, JEON J, LEE J H, *et al*. Optimal preparation of PCM/diatomite composites for enhancing thermal properties. *Int. J. Heat Mass Trans.,* 2013, **62:** 711–717.

[31] GUO S F, SHI L. Synthesis of succinic anhydride from maleic anhydride on Ni/diatomite catalysts. *Catal. Today*, 2013, **212:** 137–141.

[32] HOU Y, LAURSEN A B, ZHANG J, *et al*. Layered nanojunctions for hydrogen-evolution catalysis. *Angew. Chem. Int. Ed.,* 2013, **52(13):** 3621–3625.

[33] WANG J L, YU Y, ZHANG L Z. Highly efficient photocatalytic removal of sodium pentachlorophenate with Bi_3O_4Br under visible light. *Appl. Catal. B: Environ.,* 2013, **136–137:** 112–121.

[34] NIU P, LIU G, CHENG H M. Nitrogen vacancy-promoted photocatalytic activity of graphitic carbon nitride. *J. Phys. Chem. C,* 2012, **116(20):** 11013–11018.

[35] KHRAISHEH M A M, AL-DEGS Y S, MCMINN W A M. Remediation of wastewater containing heavy metals using raw and modified diatomite. *Chem. Eng. J.*, 2004, **99(2):** 177–184.

[36] ELZEA J M, RICE S B. TEM and X-ray diffraction evidence for cristobalite and tridymite stacking sequences in opal. *Clays & Clay Miner*, 1996, **44:** 492–500.

[37] DONG L, WU Y, SUN M, *et al*. Efficient synthesis of polymeric g-C_3N_4 layered materials as novel efficient visible light driven photocatalysts. *J. Mater. Chem.,* 2011, **21:** 15171–15174.

[38] WANG Y J, BAI X J, PAN C S, *et al*. Enhancement of photocatalytic activity of Bi_2WO_6 hybridized with graphite-like C_3N_4. *J. Mater. Chem*., 2012, **22(23):** 11568–11573.

[39] ZIMMERMAN J L, WILLIAMS R, KHABASHESKU V N, *et al*. Synthesis of spherical carbon nitride nanostructures. *Nano Lett*., 2001, **1:** 731–734.

[40] JIANG L, CHEN L L, ZHU J J, *et al*. Novel p-n heterojunction photocatalyst constructed by porous graphite-like C_3N_4 and nanostructured BiOI: facile synthesis and enhanced photocatalytic activity. *Dalton Trans.,* 2013, **42(44):** 15726–15734.

[41] ZHANG Y, THOMAS A, ANTONIETTI M, *et al*. Activation of carbon nitride solids by protonation: morphology changes, enhanced ionic conductivity, and photoconduction experiments. *J. Am. Chem. Soc.,* 2009, **131(1):** 50–51.

[42] XIAGN Q, YU J, JARONIEC M. Preparation and enhanced visible-light photocatalytic H_2-production activity of graphene/C_3N_4 composites. *J. Phys. Chem. C*, 2011, **115(15):** 7355–7363.

[43] ZHANG P F, ZHANG J L, CHEN F, *et al*. Study of adsorption and degradation of acid orange 7 on the surface of CeO_2 under visible light irradiation. *Appl. Catal. B*, 2009, **85(3/4):** 148–154.

[44] YIN M C, LI Z S, KOU J H, *et al*. Mechanism investigation of visible light-induced degradation in a heterogeneous TiO_2/eosin Y/rhodamine B system. *Environ. Sci. Technol.*, 2009, **43(21):** 8361–8366.

[45] YIN M C, LI Z S, KOU J H, *et al*. Diatomite-immobilized BiOI hybrid photocatalyst: facile deposition synthesis and enhanced photocatalytic activity. *Appl. Surf. Sci.*, 2015, **353:** 1179–1185.

[46] LI Y P, ZHAN J, HUANG L Y, *et al*. Synthesis and photocatalytic activity of a bentonite/g-C_3N_4 composite. *RSC Adv.*, 2014, **4(23):** 11831–11839.

硅藻土/g-C_3N_4 复合材料的制备及其可见光增强活性

王丹军[1], 申会东[1], 郭 莉[1,2], 何小梅[1], 张 洁[1], 付 峰[1]

(1. 延安大学 化学与化工学院, 陕西省化学反应工程重点实验室, 延安 716000; 2. 陕西师范大学 材料科学与工程学院, 西安 710119)

摘 要: 采用浸渍-焙烧法制备了具有可见光响应活性的硅藻土/g-C_3N_4 复合光催化材料。利用 TG、XRD、FE-SEM、HR-TEM、FT-IR、XPS、UV-Vis-DRS 和 PL 谱等手段对其物相组成、形貌和光吸收特性进行表征。以 RhB 的光催化降解为探针反应评价催化剂的活性。光催化结果表明, 2.32wt%硅藻土/g-C_3N_4 复合材料对 RhB 有较高的催化活性, 光催化降解的速率常数是纯 g-C_3N_4 的 1.9 倍。自由基捕获实验表明, $\cdot O_2^-$是 RhB 在硅藻土/g-C_3N_4 复合材料上光催化降解的主要活性物种。光催化活性提高的主要原因在于硅藻土和 g-C_3N_4 之间静电作用有利于光生电子-空穴在 g-C_3N_4 表面的迁移, 进而提高 g-C_3N_4 的光催化活性。

关 键 词: 硅藻土/g-C_3N_4 复合材料; 浸渍-焙烧法; 可见光照射; 静电作用

中图分类号: TB321　　**文献标识码:** A